Journal of Structural Geology 36 (2012) 55–70

Contents lists available at SciVerse ScienceDirect

Journal of Structural Geology

journal homepage: www.elsevier.com/locate/jsg

Evolution of the hourglass structures in the Laminaria High, Timor Sea: Implications for hydrocarbon traps

N. Bozkurt Çiftçi*, Laurent Langhi

CSIRO Earth Science and Resource Engineering, Box 1130, Bentley, WA 6102, Australia

ARTICLE INFO

Article history:
Received 13 May 2011
Received in revised form
7 December 2011
Accepted 12 December 2011
Available online 21 December 2011

Keywords:
Hourglass
Normal fault
Conjugate
Displacement
Mechanical stratigraphy
Fault linkage

ABSTRACT

In cross-section, an hourglass structure can be visualized as an older horst block and superimposed, younger graben. Bounding faults of the horst and graben blocks represent separate conjugate fault systems formed by two distinct episodes of extension in the Timor Sea during Late Jurassic–Early Cretaceous (1st-phase) and Middle Miocene – Pliocene (2nd-phase); with an ~120 My hiatus of limited or no fault activity in-between. Horst blocks were formed by the 1st-phase of extension and buried post-deformation. With the onset of the 2nd-phase of extension, the hourglass geometry began to form by nucleation of the graben-bounding faults in the shallow sedimentary section, in isolation from the horst-bounding faults. Location of the graben is biased by the buried horst block and graben-bounding faults grew down-dip from the shallow locus of nucleation toward the underlying horst block on which only minor reactivation occurred. Detachment of the two systems in this way was predominantly controlled by the first-order mechanical layering. A thick, shale-rich, ductile layer separates the horst- and graben-bounding fault systems and acts as a barrier to vertical fault propagation. Confinement of the graben-bounding faults into the shallow section was also facilitated by outer-arc style extension due to lithospheric flexure controlling the 2nd-phase strain in the region. The complex evolution history and the composite nature of the hourglass structures resulted in systematic along-dip variation of displacement. This variation predominantly relates to syn-kinematic deposition and location of fault tips that are controlled by the ductile layer. The presented evolution model of the hourglass structures concentrates fault tips and related stress perturbation onto the top seal and is likely to be detrimental to top-seal integrity.

1. Introduction

Normal faults with same strike but opposite dip direction are common in extensional settings and referred to as conjugate normal faults (Anderson, 1951). Conjugate normal fault systems are dominant element of the deformation pattern in the Timor Sea and form complex structures known as the hourglasses (Fig. 1) (Woods, 1988; Patillo and Nicholls, 1990). The term "hourglass" is only used as a descriptive term in this manuscript and refers to composite fault blocks with a deeper horst block generally below the Valanginian unconformity that is overlain by a shallow graben complex within the Cenozoic strata (Woods, 1988) (Fig. 2). Hourglasses attract exploration interest in the Timor Sea (Fig. 3) with hydrocarbons typically trapped in the deeper horst blocks (Woods, 1992; Smith et al., 1996). Yet, cases of trap breaching with partial or complete loss of hydrocarbon columns are known and noted as the principal exploration risk in the area (Lisk et al., 1998; O'Brien et al., 1999; De Ruig et al., 2000; Gartrell et al., 2005, 2006; Langhi et al., 2010). Hence, understanding of the evolution and deformation style of the hourglass structures is critical to effective risk management.

Studies from the Timor Sea traditionally attributed the hourglass geometry imaged on the seismic profiles to crossing of oppositely dipping conjugate normal faults (Fig. 1) (Woods, 1988; Nicol et al., 1995; Bretan et al., 1996; Gartrell et al., 2005). Operation of crossing conjugate normal faults has been the subject of previous studies and several models have been proposed for the kinematics of the intersecting pairs. Ramsey and Huber (1987) noted that simultaneous operation of crossing conjugate normal faults brings a compatibility problem around the intersection zone requiring modification of the cross-sectional area (or volume in three dimensions). They concluded that the compatibility problem can be avoided by sequential slip of the intersecting pairs. Nicol et al. (1995) investigated these structures in Cartier Trough (Fig. 3) and concluded that crossing conjugate normal faults slip

* Corresponding author. Tel.: +61 (08) 64368794.
E-mail address: Bozkurt.Ciftci@csiro.au (N.B. Çiftçi).

0191-8141/$ – see front matter © 2011 Elsevier Ltd. All rights reserved.
doi:10.1016/j.jsg.2011.12.006

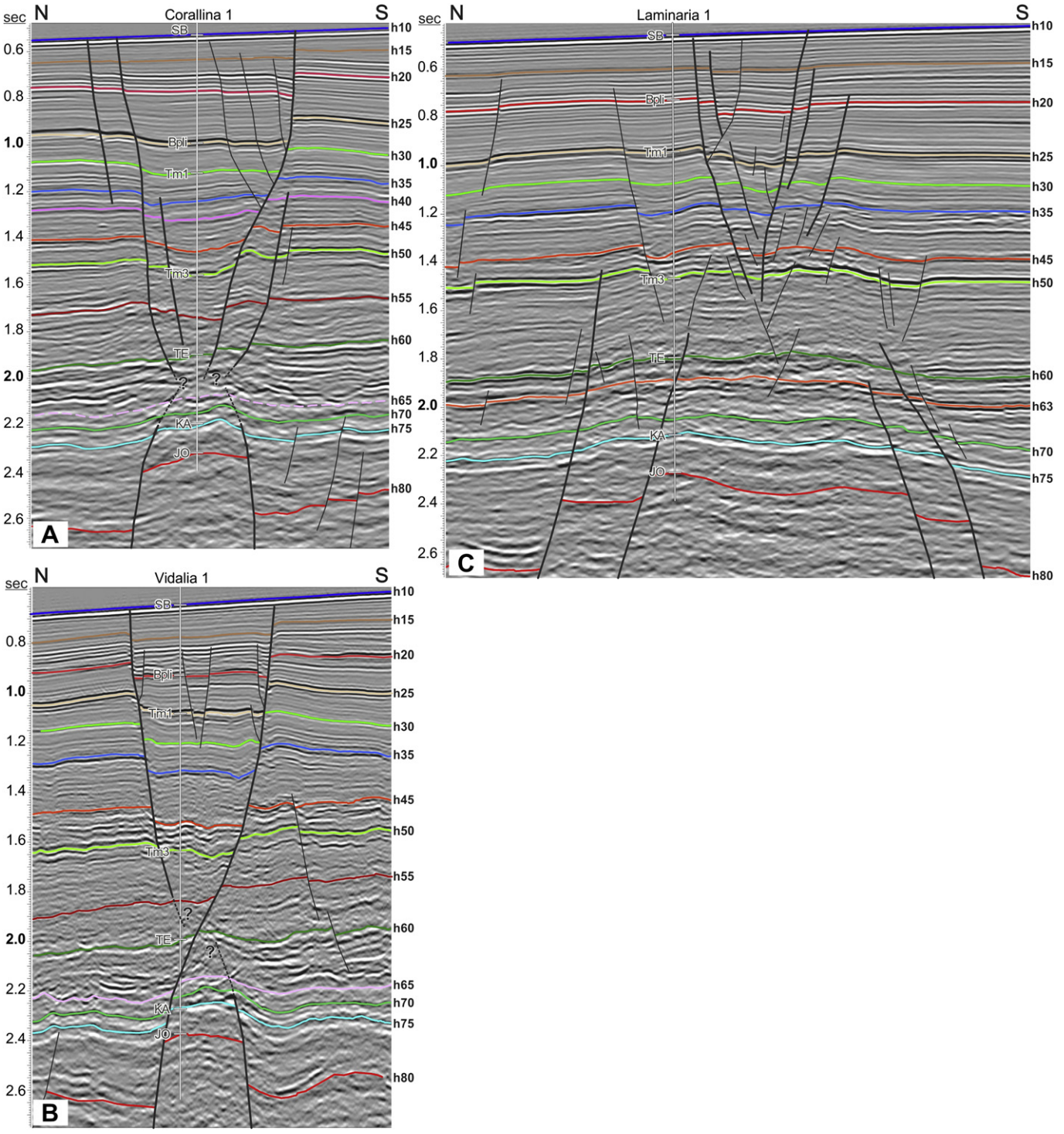

Fig. 1. Transverse seismic profiles across the hourglass structures: (A) Corallina; (B) Vidalia; and (C) Laminaria structures with horizon and fault interpretations. Bold faults represent the faults included in throw analysis (see text for details). Vertical scale is TWT in seconds. Horizon names h10–h80 are the naming convention used in this study and well picks illustrates age of the corresponding horizon. Note that there is vertical exaggeration due to vertical axis being in time domain. Well pick abbreviations: JO – Oxfordian; KA – Aptian; TE – Eocene; Tm3 – Base Miocene; Tm1 – Late Miocene; Bpli – base Pliocene; SB – sea bed (Fig. 2).

simultaneously and the kinematic incompatibility is accommodated by a systematic reduction of displacement and a corresponding increase in ductile strain (at the scale of seismic data) toward the intersection zone. Watterson et al. (1998) presented outcrop examples to illustrate that the vertical displacement gradients and increase in strain toward the intersection zone can be accommodated by intergrain slip, volume decrease or multiple smaller scale faults. Ferrill et al. (2000, 2009) showed that truly simultaneous activity of crossing conjugate normal faults is limited to extremely small displacements due to rate limiting area change process. Alternating, sequential slip on crossing pairs resolves this constrain without a need for an area change and can be used to restore even the most complicated crossing conjugate normal fault patterns (Ferrill et al., 2000; Çiftçi and Bozkurt, 2009).

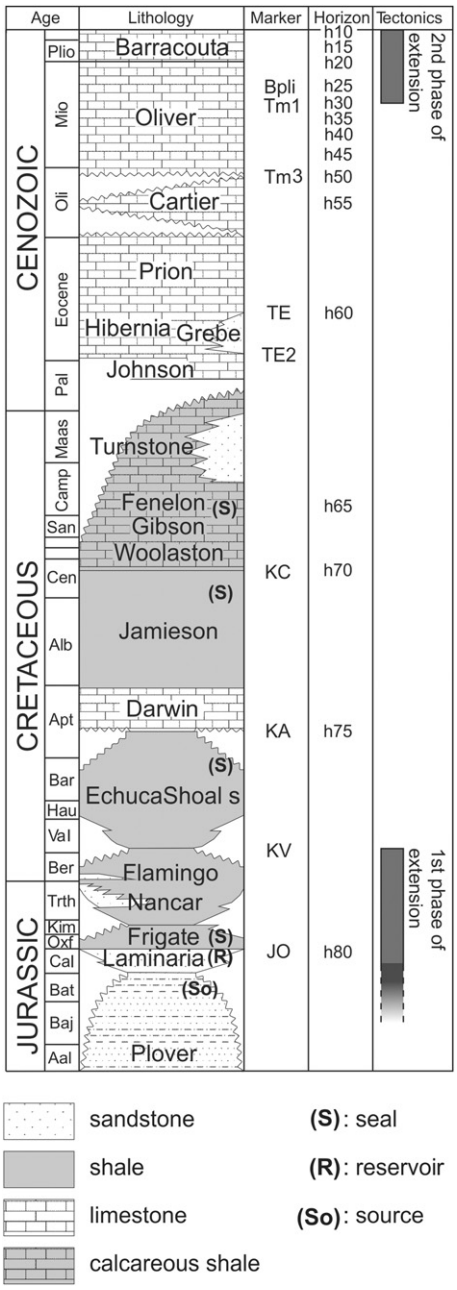

Fig. 2. Stratigraphic column of the Laminaria High area. Periods of 1st- and 2nd-phases of extension, seismic stratigraphic markers, interpreted horizons and main source-reservoir-seal intervals are also illustrated. Modified from De Ruig et al. (2000).

Although these models provide viable explanations to operation of crossing conjugate normal faults and may be relevant to hourglass structures in some parts of the Timor Sea (e.g., Nicol et al., 1995), the examples in the Laminaria High area can be distinguished from them based on some basic observations. The horst- and graben-bounding conjugate normal faults represent two different fault systems which have formed by two different phases of extension with different stress fields and a ~120 My time gap (1st- and 2nd-phases of extension in Fig. 2). During the 2nd-phase of extension, the two systems might have connected vertically with reactivation of the older system and formed geometry similar to crossing conjugate normal faults (e.g., Fig. 1B). However, the deformation style of the entire hourglass structure cannot be simply explained by crossing conjugate normal faults models as this geometry formed ~120 My after the main deformation phase of the deeper horst block. Furthermore, the displacement variation on the faults does not correlate to crossing conjugate normal fault geometry but relates to the composite deformation characteristics of these structures.

The aim of this study is to improve the understanding of the hourglass structures over the Laminaria High area based on the data from Corallina, Vidalia and Laminaria structures (Figs. 3 and 4). To accomplish this, syn-kinematic intervals and first-order mechanical stratigraphic units were differentiated in the stratigraphic column and the displacement distribution was mapped on the bounding fault surfaces. We show that the variation of displacement is related to syn-kinematic stratigraphic expansion and mechanical boundaries in the sedimentary column. The assessment of displacement distribution suggests a detached evolution of the graben and horst-bounding faults which may or may not be connected depending on the local geology. This evolution has implications in evaluation of hydrocarbon trap integrity in the area. Inferences may also be relevant to other areas possessing similar fault pattern, vertically detached fault systems or mechanically anisotropic stratigraphic column.

2. Geological setting

The Australian North West Shelf is one of the main hydrocarbon provinces of Australia and comprises four main compartments (Fig. 3): Carnarvon, offshore Canning, Browse and Bonaparte basins (Purcell and Purcell, 1988). These Phanerozoic basins are collectively referred as the Westralian Superbasin (Yeates et al., 1987) and represent basement involved segmentation with strong geological similarities among the basins. Bounded by the Banda-Timor orogen to the north, Argo Abbysal Plain to the west and Proterozoic craton and basins to the south, the North West Shelf evolved through series of major rifting phases and host thick sequences of Paleozoic, Mesozoic and Cenozoic sediments (AGSO, 1994; Baillie et al., 1994; Longley et al., 2002; Borel and Stampfli, 2002). The dominant NW–SE structural trend is the product of the Late Jurassic–Early Cretaceous rifting (i.e., 1st-phase of extension) of the Argo abyssal plain (Fig. 2) (AGSO, 1994; Baillie et al., 1994).

The Laminaria High is located at the north of the Bonaparte Basin adjacent to the shelf-slope break (Fig. 3). It represents a platform–remnant bounded by the Flamingo Syncline and the Nancar Trough (Smith et al., 1996). The structural grain here is predominantly E–W-oriented and deviates from the regional NE–SW trend although both were inherited from the 1st-phase rifting (Figs. 3 and 4). This phase was followed by the postrift subsidence through the rest of the Mesozoic and most of the Cenozoic era. From the Miocene onward, the Timor Sea was intensively influenced by the collision between the Australian and Eurasian plates along the Banda-Timor orogen (O'Brien et al., 1993). This triggered the 2nd-phase of extensional deformation in the area (Fig. 2); probably due to thrust loading around Timor Island and consequential lithospheric flexure of the Australian plate margin (Fig. 3) (Bradley and Kidd, 1991; Langhi et al., 2011). The onset of the collision is dated to the Late Miocene at approximately 8 Ma (Shuster et al., 1998; Charlton, 2000; Keep et al., 2002) with a second pulse occurring during the Pliocene at ~4–3 Ma (Charlton et al., 1991).

The stratigraphic column reflects the 1st-phase rifting and the following passive margin evolution in the region (Fig. 2). The early syn-rift Plover and Laminaria formations, which represent deltaic and shallow marine deposition (Labutis et al., 1998), are overlain by the Late Jurassic to Cretaceous shales (Frigate, Flamingo and Echuca Shoals formations) of the deepening continental shelf (Whittam et al., 1996). The Aptian–Maastrichian interval (Darwin, Jamieson, Woolaston, Gibson, Fenelon and Turnston Formations) comprises

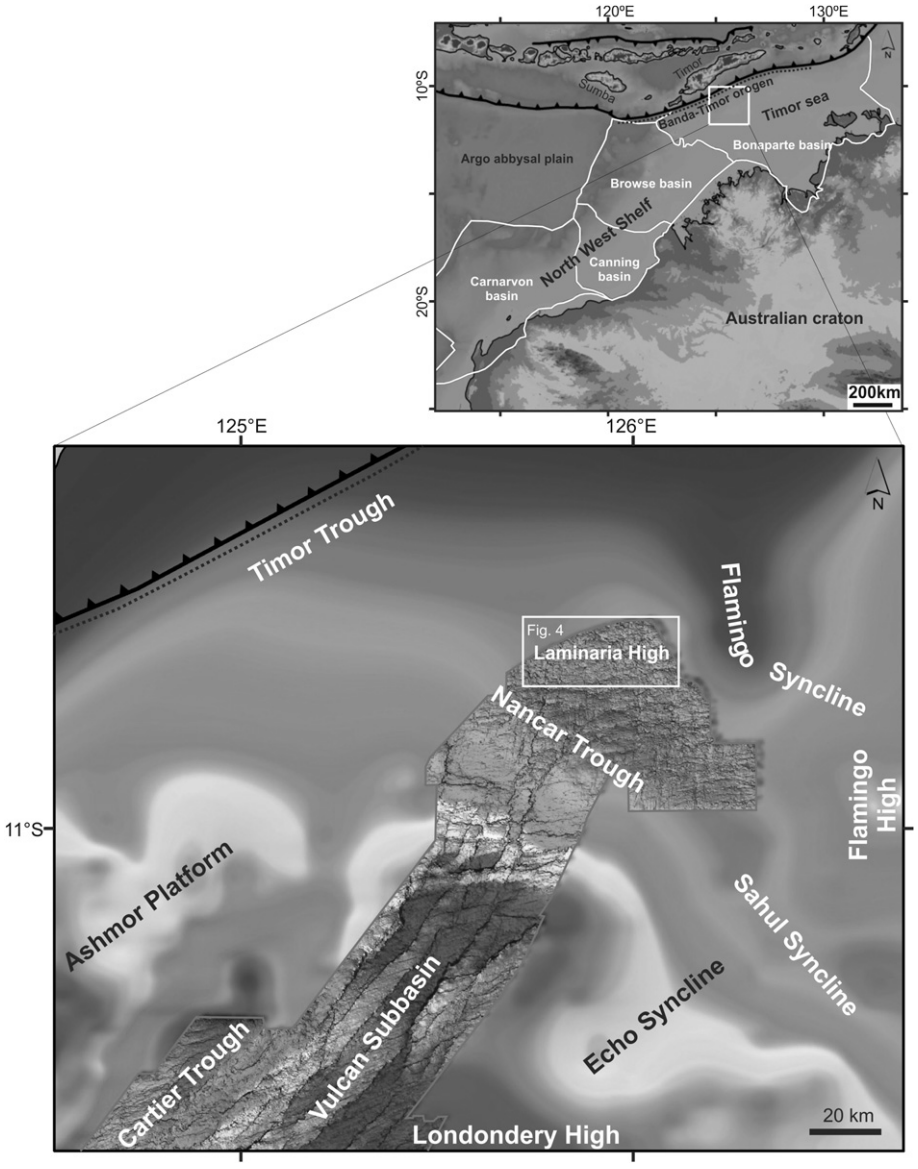

Fig. 3. Simplified location map and main structural domains around the study area. Gray shading depict the structure of top Permian horizon (modified from Edwards et al., 2005). Inset map illustrates main compartments of the Australian North West Shelf and the surrounding area.

stacked progradational wedges of silty claystone cleaning up to calcareous shale and marl-prone sediments (Whittam et al., 1996). As the wedges fill up the accommodation created by the subsiding margin, carbonate content increases and monotonous succession of silty claystones grades upward into calcareous claystone, calcilutite and marls. An extensive cover of prograding shelfal carbonates (Johnson, Hibernia, Prion, Cartier, Oliver and Barracouta formations) deposited during the Cenozoic to represent the mature phase of the passive margin.

Hydrocarbons are typically reservoired in the Callovian Laminaria Formation and sealed by the overlying thick section of shales and silty claystone (Fig. 2). Source rocks are found in the Plover Formation and Frigate shales (Preston and Edwards, 2000; George et al., 2004). An initial early gas charge is suggested during the Late Jurassic–Early Cretaceous in response to the elevated heat flow during the rifting (Lisk et al., 1998). The main hydrocarbon charge occurred near the middle to late Eocene (~50 Ma), with possible late-stage gas and oil charges during renewed subsidence from the Miocene onward (Kennard et al., 1999).

3. Methodology

Analyses in this study are predominantly based on the stratigraphic and structural interpretations of the Laminaria 3D seismic survey. This survey was acquired in 1995 with an approximate coverage of 760 km^2 and was shot in an E–W direction using 12.5 × 25 m asymmetric binning (De Ruig et al., 2000). The data has been processed and post stack depth migrated sections are available for interpretation with an SEG negative polarity.

Our interpretation was focused on the Laminaria, Corallina and Vidalia hourglass structures (Fig. 4). Faults were initially picked manually on every 5th cross-lines (125 m) that are oriented orthogonal to the structural trend. This interpretation was guided by extraction of a full resolution (12.5 × 25 m) coherency cube along horizons and time slices. This allowed accurately mapping the fault traces and correlating fault segments up to the limit of the seismic resolution. Faults which can be traced more than 500 m along-strike were included in the interpretations.

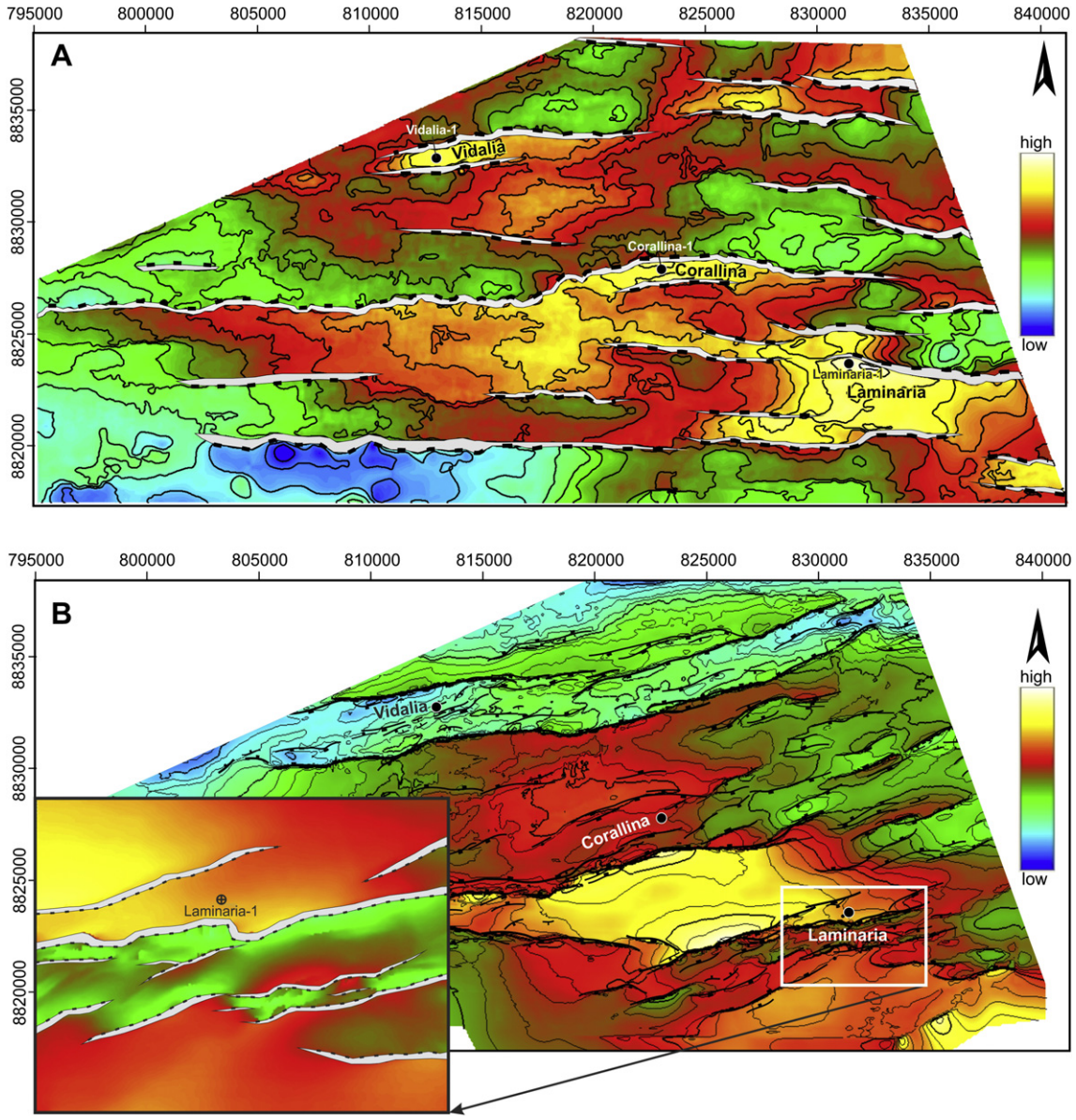

Fig. 4. Maps showing fault patterns in the Laminaria High area with locations of Vidalia, Corallina and Laminaria structures. See Fig. 3 for the location of maps in the North West shelf. (A) Time structure map of Late Jurassic horizon (h80 in Fig. 1) illustrating the older horst blocks; and (B) time structure map of the Base Pliocene horizon (h20 in Fig. 1) illustrating the younger grabens of the hourglass structures. Coordinate grid is UTM Zone 51S.

Horizons were also picked manually on every 5th cross-line and every 20th in-line (250 m) and the manual horizon picks were fed into an automated horizon hunt algorithm for continuous picking through the volume. That was followed by quality control of the horizon interpretations and touch ups, especially around fault cuts. Every horizon that can be correlated across the faults and traced with confidence was included in the interpretation with total up to 15 horizons from sea bed to top reservoir interval (Figs. 1 and 2).

Horizon and fault interpretations were exported into 3D modeling software where the time-domain seismic interpretations were depth converted using multi-layered velocity model. Each hourglass structure was treated separately using a single well located on the horst block. Velocities for layers were selected under the control of this well to provide the best match between the horizons and the corresponding well picks. Once the fault and horizon data were brought into the depth domain, 3D models were built and fault-horizon cut-offs were computed to constrain displacement distributions. Isochore maps were extracted between consecutive horizon pairs and examined for syn-kinematic sections with stratigraphic thickening on the hangingwalls. Various cross-sections extracted from the models were used to assess the observed trends in displacement distributions and their relations to syn-kinematic sections.

Given a sound fault/horizon interpretation, the largest error for the described workflow is likely to be sourced by the time to depth conversion. Tying each structure to a single well will produce an error increasing away from the well due to lateral variation of the velocity. We assumed that this lateral variation can be ignored at the scale of this study. The modeling errors also remain insignificant at first-order and are unlikely to alter the observed geological trends.

4. Phases of extension and related syn-kinematic deposition

Periods of syn-kinematic deposition can be defined based on the variation of stratigraphic thickness across the hangingwall and footwall blocks. For this purpose, isochore maps were extracted

between interpreted horizons (Fig. 5). Although an isochore map indicates vertical thickness, the low stratigraphic dip associated with the investigated hourglass structures allows us to use this information as a proxy for stratigraphic thickness (Fig. 1). We averaged the isochore thickness across 2-km wide belt along the fault for hangingwall and footwall blocks to compute the hangingwall to footwall thickness ratio (Fig. 5). Fig. 6 illustrates this ratio that was plotted against each layer for north- and south-dipping faults.

Two main periods of syn-kinematic deposition can be recognized on Fig. 6. They are shaded as gray areas where the hangingwall/footwall thickness ratio is consistently above 1.0 for both north- and south-dipping faults of the three structures. These periods occur below h75 and above h30 and correlate to the regional 1st- and 2nd-phases of extension, respectively. Therefore, we will refer to these intervals as 1st and 2nd syn-kinematic packages. Note that the average fault orientation varies between the 1st and 2nd syn-kinematic packages as much as 20° (Figs. 4 and 6).

The Valanginian unconformity (KV) is associated with the end of syn-rift deposition for the 1st-phase of extension (Fig. 2) (Longley et al., 2002). This unconformity occurs only 20–35 m below the h75 and is probably included within the seismic response of this horizon (Fig. 1). Thickening of the h70–h75 interval on the hangingwalls is predominantly related to passive filling of the remaining accommodation space following the demise of the 1st-phase of extension. This interval can be linked to 1st syn-kinematic package but it represents deposition over surface relief and burial of the ceased 1st-phase structures (Fig. 6).

The stratigraphic interval between h70 and h30 indicates no consistent change in the hangingwall thickness relative to footwall with thickness ratio clustering around 1 (Fig. 6). This indicates that the stratigraphic interval was deposited in quiescence without any fault activity.

5. Mechanical stratigraphy

Faulting in sedimentary rocks can be influenced by mechanical stratigraphy caused by varying competency and thickness of the layered units (e.g., Wilkins and Gross, 2002; Ferrill et al., 2007; Ferrill and Morris, 2008; Morris et al., 2009). Mechanical stratigraphic units can possess varying style and intensity of deformation within the same column of rock and under the same stress conditions. Mechanical stratigraphic units do not necessarily correlate to lithostratigraphic units but closely relates to gross lithic properties which control the mechanical response of rock to stress (e.g., Donath, 1970).

The sedimentary column associated to the hourglass structures can be divided into three key lithic units dominated by limestone, shale and sandstone, respectively (Fig. 7). These units have significant thicknesses and are laterally extensive at the basin scale. Variation of uniaxial compressive strength (UCS) across these units was computed using P-wave sonic logs from a borehole over each structure (Fig. 7). This computation is based on the empirical correlation between slowness and UCS proposed by Horsrud (2001). UCS values correlate to the gross lithological divisions and suggest that these units are likely to behave as three distinct mechanical stratigraphic units (MU). Limestone dominated shallowest MU-1 is a competent unit with thickness exceeding 2000 m and UCS of the interval averaging around ~27 MPa (ranges from ~17 to 40 MPa). Note that sonic log coverage of this unit is not complete resulting in partial UCS computation. MU-1 is underlain by an incompetent shale dominated MU-2 with thickness around 500 m and average UCS of ~18 MPa (ranges from ~10 to 29 MPa). Sandstone dominated and competent MU-3 is located at the base of the drilled section with an average UCS of ~24 MPa (ranges from 20 to 27). Maximum drilled thickness of this unit is ~400 m in Vidalia-1, but it is likely to extend further below the drilled section.

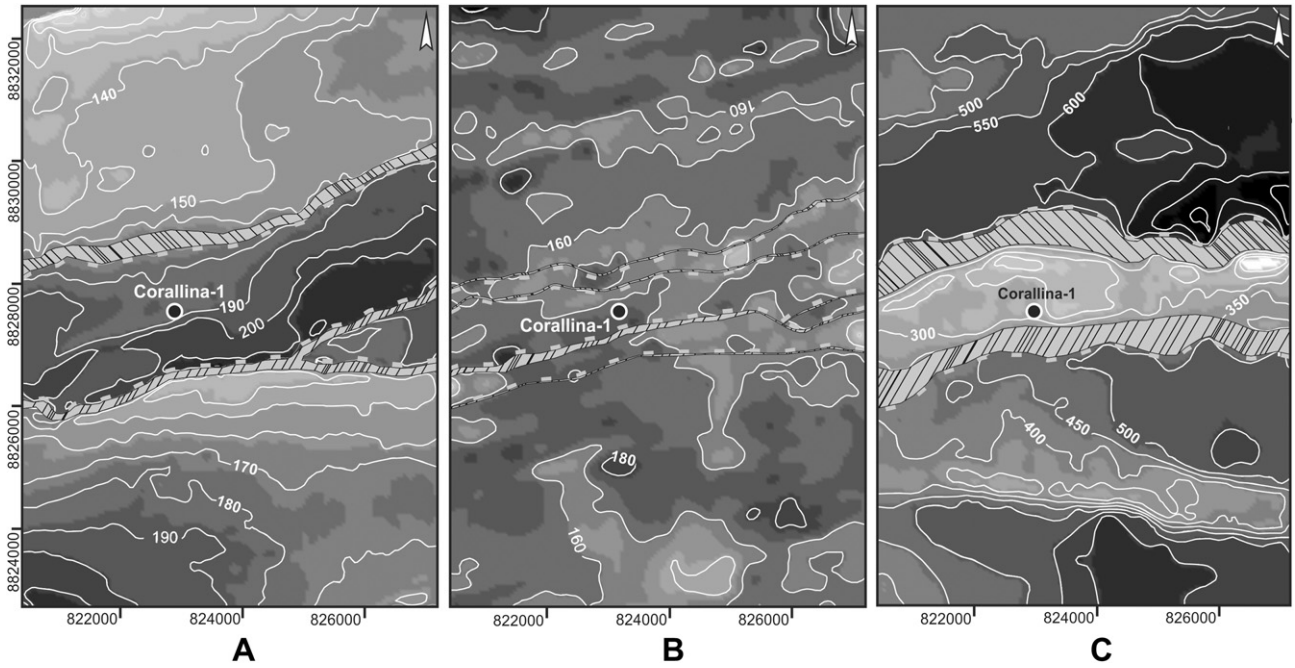

Fig. 5. Illustrative examples of isochore maps from the Corallina structure. Isochores increase toward the darker shades and tick marks on the faults depict hangingwall blocks. (A) Between h20 and h25 – contour interval is 10 m; (B) between h45 and h50 – contour interval is 20 m. The graben block here was defined between the northernmost and southernmost faults; and (C) between h75 and h80 – contour interval is 50 m. Refer to Figs. 3 and 4 for age and position of the horizons within the hourglass structure.

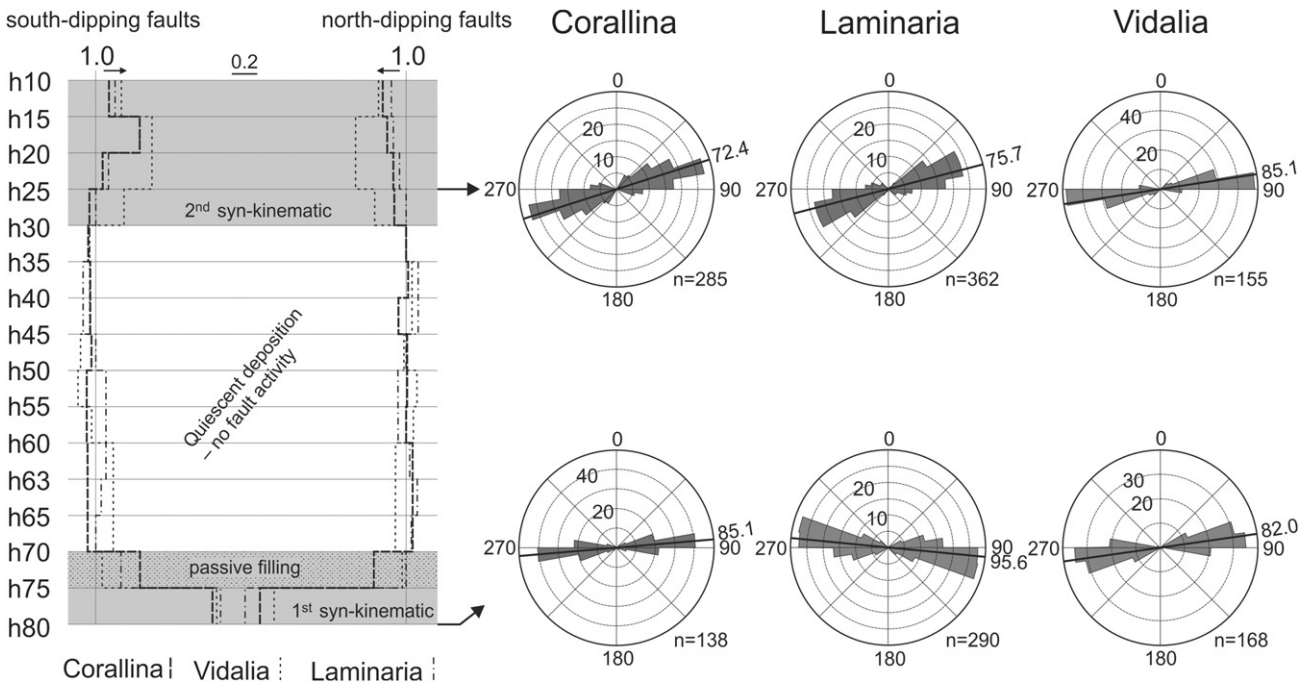

Fig. 6. Plot showing the hangingwall to footwall thickness ratio with respect to north- and south-dipping faults of the Corallina, Laminaria and Vidalia structures. The ratio is consistently >1 below h70 and above h30 marking 1st- and 2nd-phases of syn-kinematic deposition (gray shaded areas). Rose diagrams depicts orientation of faults cutting h80 (lower row) and h25 (upper row) horizons. Length of petals is scaled to number of strike measurements (100 m apart) along the footwall cut-off of the related horizon.

6. Geometry of the hourglass structures

The faults bounding the hourglass structures are referred to as 1st- and 2nd-phase fault systems to link them to related deformation phase and syn-kinematic deposition (Fig. 8). It is difficult to make this distinction precisely due to two reasons: (i) There is reactivation and perhaps upward propagation of the 1st-phase faults during the 2nd-phase of extension; and (ii) faults of 1st- and 2nd-phases can be connected to form a composite structure with different segments belonging the different phases. For simplicity, however, we will bind the 1st-phase faults by the top of the 1st syn-kinematic package and refer any fault beyond as the 2nd-phase faults (Fig. 8). This discrimination will be justified in the next sections.

6.1. 1st-phase faults

The 1st-phase faults are the main system forming the E–W-oriented fabric in the area (Fig. 4A). They comprise oppositely dipping, conjugate fault sets and form series of E–W trending horsts and intervening grabens with highly segmented spatial distribution. Fault dips are generally in the range of 60–65°, although the dip can vary to 45–50° locally. The horst blocks generally define the bases of the hourglass structures (Figs. 1 and 8). Their width varies from ~1 km (e.g., Vidalia and Corallina structures) to ~5 km (e.g., Laminaria structure) at the Late Jurassic h80 horizon (Fig. 4A). The along-strike extent of the individual 1st-phase faults varies from 2 to 30 km but the associated horst blocks generally extend in the range of 7–12 km. They dip toward east and west to merge into more subtle larger scale horst blocks. Horst blocks can be asymmetric or tilted (e.g., Corallina structure) with displacement differing among the bounding structures. Offsets exceeding 500 m are common on these faults and considerable thickening of the stratigraphic section is notable on their hangingwalls through the 1st syn-kinematic package (Figs. 5C and 8).

6.2. 2nd-phase faults

The grabens bounded by 2nd-phase faults generally superimpose the horst blocks bounded by 1st-phase faults (Fig. 4B). The structural trend could deviate in the younger system and the faults carry relatively less displacement (<200 m) (Figs. 4 and 8). Yet, they are still influential on the distribution of stratigraphic thickness within the shallow section (Figs. 5A and 6). The subsidence of the graben blocks can be asymmetrically distributed between the north- and south-dipping faults with single or multiple bounding faults (Fig. 1). Second order synthetic and antithetic faults are common within the hangingwall. The fault system has low structural maturity and generally comprises short, overlapping segments with intervening relay ramps (Fig. 4B). Hence the intervening graben blocks may not be well defined spatially in contrast to the underlying horst blocks.

The deformation style of the 2nd-phase grabens varies slightly between the studied structures: (i) An asymmetric graben is formed in the Corallina structure with the north-dipping fault accommodating a larger part of the 2nd-phase strain; this fault is also associated with a series of antithetic faults (Fig. 1A and 8A); (ii) the graben of the Vidalia structure displays two principal conjugate segments with slight asymmetric distribution of strain and few associated small antithetic faults (Figs. 1B and 8B); and (iii) the Laminaria graben represents a cluster of 2nd-phase faults with two main segments and a series of subordinate antithetic and synthetic faults (Figs. 1C and 8C).

1st- and 2nd-phase faults approach each other around the h60–h70 interval above the 1st syn-kinematic package (Fig. 8). Vertical kinematic coherency between the two systems varies widely between the soft-linked and hard-linked end members. It can be observed that the 2nd-phase extension resulted in some reactivation of the 1st-phase faults and the reactivation offsets can be resolved on the post 1st-phase horizons such as h70 (Fig. 8). These reactivations can extend the 1st-phase faults above the 1st

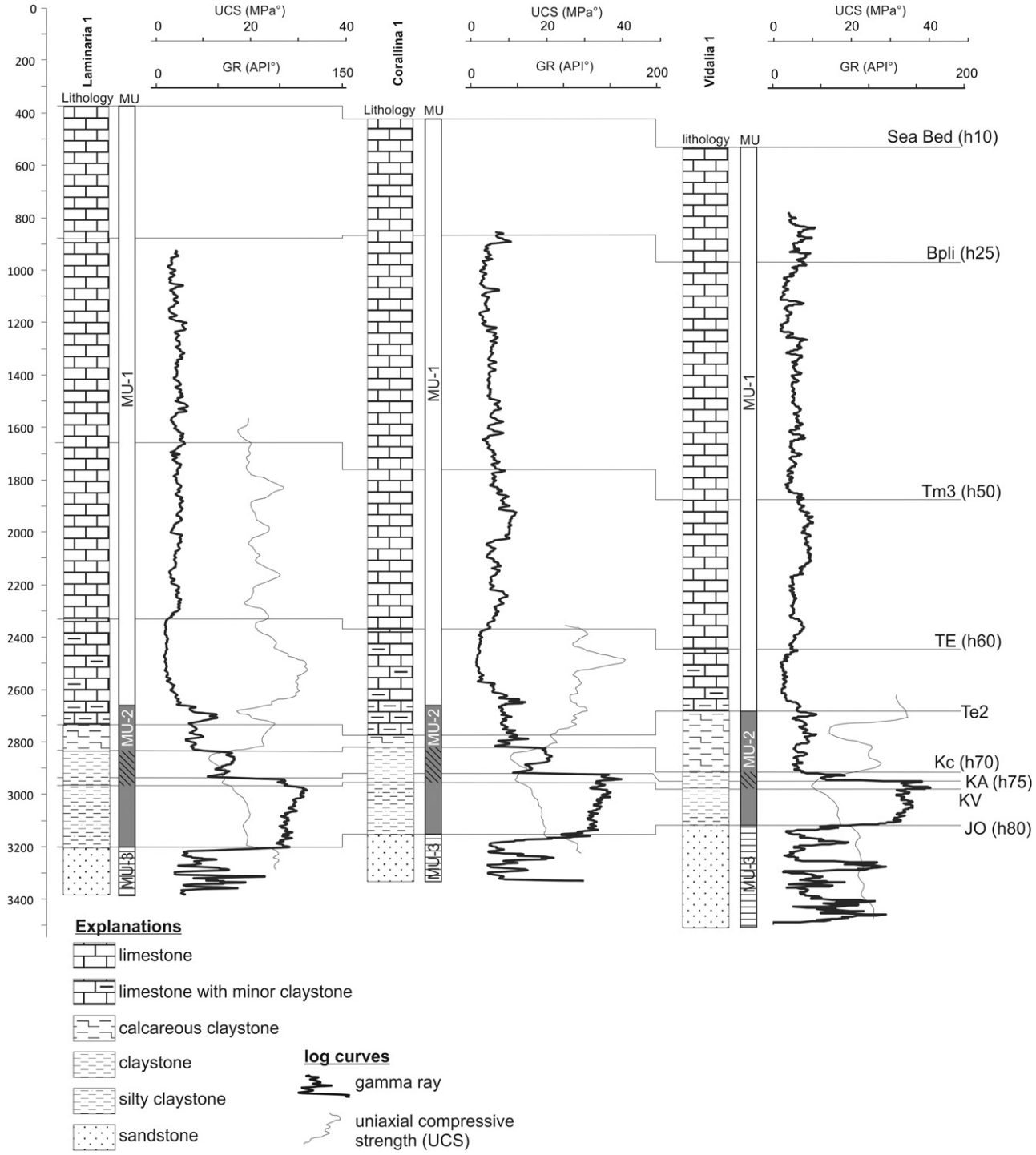

Fig. 7. Stratigraphic columns of the three hourglass structures depicted by Laminaria-1, Corallina-1 and Vidalia-1 wells. Lithology, mechanical stratigraphic units (MU), gamma ray log (GR) and uniaxial compressive strength (UCS) computed from p-wave sonic logs (Horsrud, 2001) are illustrated. Some of the key horizons depict the correlation between the wells and stratigraphic location of the MUs. Note that competent MU-1 and MU-3 are separated by incompetent MU-2. Hatched interval of MU-2 depicts the weakest section of the unit.

syn-kinematic package. However, the reactivation amount varies among the structures and generally remains minor compared to the maximum offset of the 2nd-phase faults.

7. Analysis of displacement distribution

Displacement or slip on a fault surface can be resolved into vertical and horizontal components referred to as throw and heave, respectively. Analysis of the fault slip and its components in the Laminaria high area indicates systematic variation of fault displacement (Fig. 8). Slip profiles clearly depict two displacement maxima (t_{max1} and t_{max2}) that are separated by a distinct displacement minimum (t_{min}). All the slip anomalies consistently occur around the same stratigraphic level for the three structures although slight along-strike variations exist (Fig. 9). Throw patterns closely follows the slip patterns due to steep fault dips and captures the displacement variation along the structures (Fig. 8). Therefore, we generally use the throw as a proxy to the displacement. Note

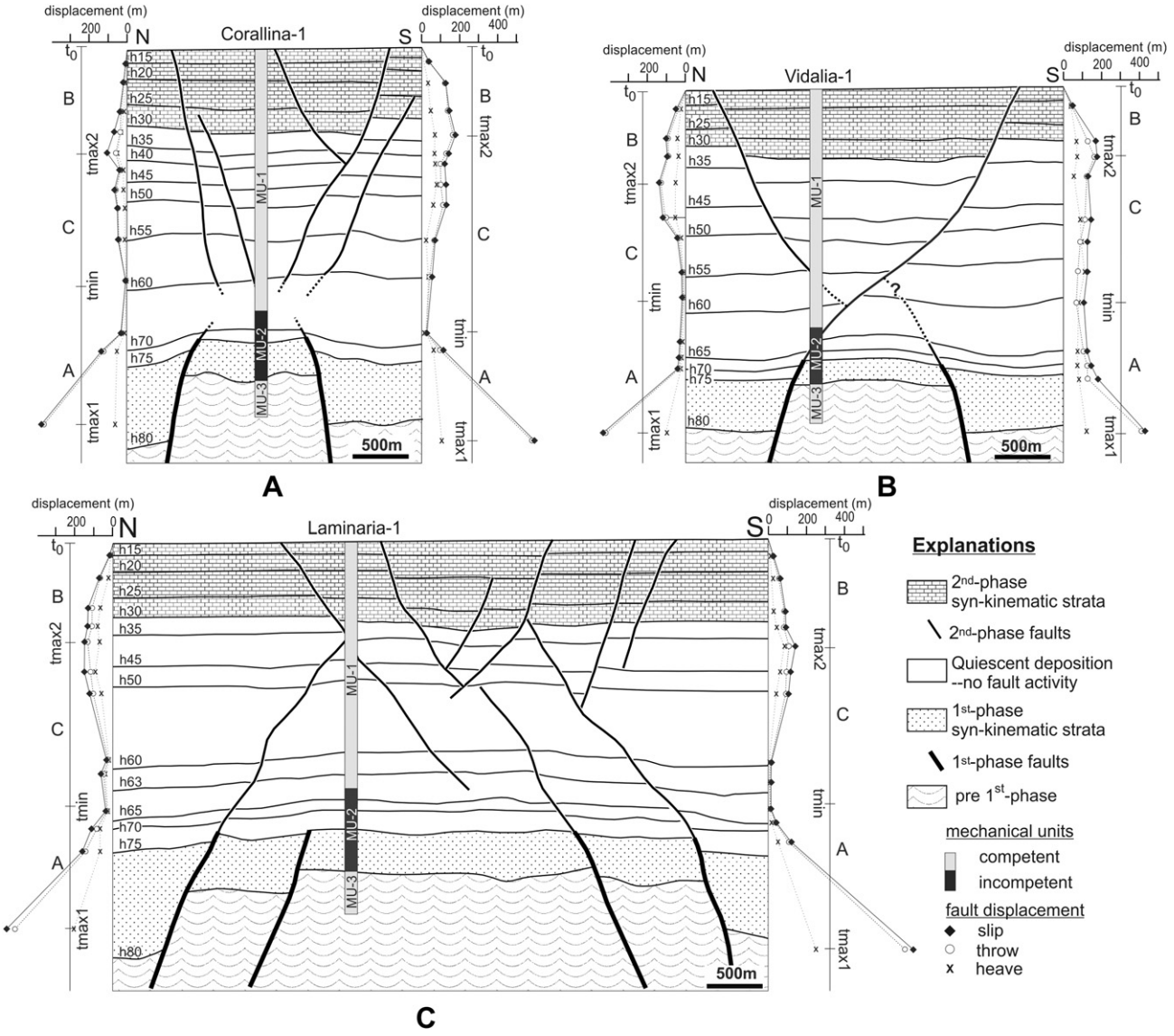

Fig. 8. Geological cross-sections illustrating the hourglass structures: (A) Corallina, (B) Vidalia; and (C) Laminaria structures. Faults and syn-kinematic packages formed by 1st- and 2nd-phases of extension are illustrated on the cross-sections. Displacement distributions are plotted on the right and left side of the each cross-section for north- and south-dipping faults, respectively. Each throw profile was divided into throw domains (A, B, C) which were discussed in detail in the text. No vertical exaggeration.

that the slip profiles are cumulative for the overlapping synthetic fault segments.

t_{max1} is associated with the 1st-phase faults and MU-3 with displacements exceeding 500 m as observed on the horizon h80 (Figs. 8 and 9). Up-dip from t_{max1}, the throw decreases within MU-2 along with the 1st syn-kinematic package down to a minimum value (t_{min}) near the top of MU-2 (Fig. 8). Between t_{min} and the present-day seafloor (t_0), several small scale displacement peaks and troughs are observable within the MU-1 (Fig. 9). However, these relative variations are not consistent among the adjacent profiles and another displacement maximum can be defined at t_{max2} (Figs. 8 and 9). Displacement at t_{max2} is smaller than t_{max1} and rarely exceeds 200 m. t_{max2} generally occurs near h35 slightly below the 2nd syn-kinematic package. Throw decreases up-dip within the 2nd syn-kinematic package and dies off at the present-day seafloor at t_0. Similarly, throw decreases down-dip away from t_{max2} and drops to minimum at MU-2.

The observed throw profiles form three main domains possess different throw gradients (i.e., the rate of throw change per stratigraphic thickness along the fault; Fig. 10). We use positive and negative gradients to represent down-dip increase and decrease of throw, respectively. Domain A covers the interval between t_{min} and t_{max1} and is characterized by positive gradient reaching up to 0.95 with an arithmetic average of 0.58. This suggests a throw decrease of 58 cm in average per meter of stratigraphic section. The gradient in domain B is also positive between t_{max2} and t_0 with a relatively lower average of 0.20. The throw gradient in domain C is negative corresponding to down-dip decrease of throw from t_{max2} to t_{min}. The gradient average of −0.12 in this domain is distinctly smaller than the gradients observed through domains A and B.

The above discussion relates to the observed present-day throws which can deviate from the actual throws at the time of faulting due to compaction of sediments. The impact of compaction is likely to be more significant within the syn-kinematic packages where faulting occurred in poorly compacted sediments that are subsequently buried. Largest deviation is expected in the 1st syn-kinematic package with burial depth above 3000 m. Taylor et al. (2008) modeled displacement loss as a function of

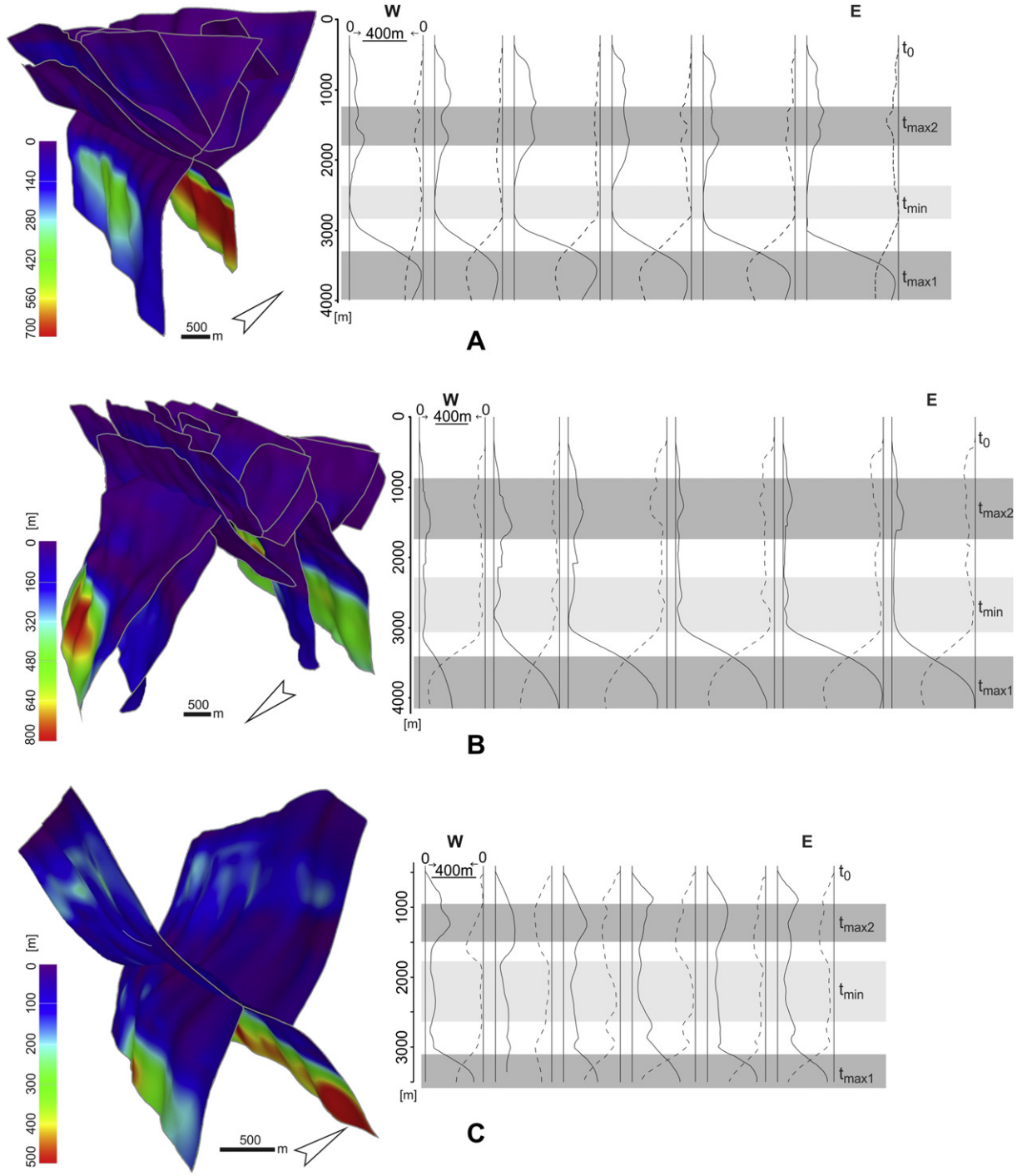

Fig. 9. Fault models and throw distributions for Corallina (A), Laminaria (B) and Vidalia (C) structures. Throw profiles were extracted 1 km apart along each structures and depicts vertical distribution of cumulative throw on north-dipping (solid line) and south-dipping (dashed line) faults. 1st- and 2nd-phase faults were modeled as continuous surfaces as possible to capture the variation of throw although they may not be connected (Fig. 8). Zero throw zones on the fault surfaces depict areas where the faults are disconnected or segmented.

depth for various lithologies and growth indices where the growth index is defined as the ratio of the difference in hangingwall and footwall thicknesses divided by the footwall thickness. As growth indices are generally around or exceed 1 for the 1st syn-kinematic package, displacement loss due to compaction hardly reaches 10% at the current burial (Fig. 6 in Taylor et al., 2008). The deviation is likely to be less through the carbonate dominated 2nd syn-kinematic package. Compaction related displacement loss is probably insignificant in the h50–h70 interval because faulting in this interval occurred during the 2nd-phase after considerable burial.

8. Discussions

8.1. Displacement distribution

Displacement distribution provides insight into the propagation and slip history of faults (Walsh and Watterson, 1987, 1988; Cowie

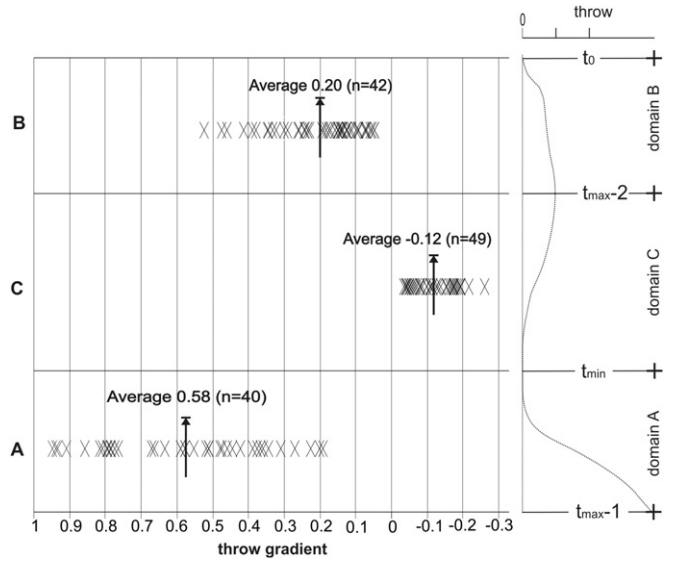

Fig. 10. Generalized vertical throw gradients observed on the hourglass structures. Three distinct throw domains (A–C) can be defined based on the direction and gradient of throw change. Down-dip increase and decrease of throw are illustrated by positive and negative gradients, respectively.

and Scholz, 1992). It is also useful to reconstruct the evolution history of segmented or composite structures (Childs et al., 1995, 1996; Morley, 1999). An ideal displacement distribution on a single, blind, normal fault surface can be described by a zone of maximum at the fault center that decreases to zero radially in all directions (Barnett, et al., 1987; Walsh and Watterson, 1988). A displacement profile can portray this distribution with a centrally located zone of maximum (Fig. 11A). It is a common assumption that the fault nucleates at this zone of maximum displacement as parts of the fault near the tips have undergone less slip compared to the zone of nucleation (Walsh and Watterson, 1987; Childs et al., 1993; Wilkins and Gross, 2002; Meyer et al., 2002). Accordingly, a gradient arises away from the maximum in up- and down-dip directions to account for the demise of displacement at the fault tips and relates to tip propagation gradients (Fig. 11A) (Cartwright and Mansfeld, 1998; Wilkins and Gross, 2002; Walsh and Watterson, 1987). Low and regular displacement gradient is commonly associated with blind fault tips (e.g., Meyer et al., 2002; Baudon and Cartwright, 2008b).

On a growth fault reaching to the free surface, a displacement plateau forms between the point of maximum displacement and the free surface (Fig. 11B). Syn-kinematic stratigraphic expansion initiates at the upper tip of the fault (Fig. 11C). Due to thicker deposition on the hangingwall block, displacement gradually diminishes upward in the syn-kinematic section given that the sedimentation rate keeps pace with rate of displacement (e.g., Taylor et al., 2008; Baudon and Cartwright, 2008a,b). The associated displacement gradient could be variable depending on the rate of sedimentation and can be differentiated from the tip related gradients based on the knowledge of syn-kinematic strata.

8.2. Evolution of the hourglass structures in the study area

The steep positive gradient in domain A correlates with the 1st syn-kinematic package (Figs. 8 and 10). The high gradient value in this domain (reaching up to 0.95) is unlikely to be accommodated in crustal conditions unless there is a volume change across the fault plane. The required volume change was effectively provided by the syn-kinematic strata in the form of thicker stratigraphic section on the hangingwall. This suggests that the displacement distribution along the horst-bounding faults was predominantly controlled by an initial stage in the evolution of the hourglass structures that comprised the formation of the 1st-phase fault system, the deposition of 1st syn-kinematic package and the passive filling of the remaining accommodation after fault activity ceased (Fig. 12A).

The influence of the 1st-phase fault system on the deposition was probably terminated by h70. Lack of any syn-kinematic section between h70 and h30 (Fig. 6) suggests that the deposition took place at structurally quiescent conditions through the interval without significant relief on the free surface (Fig. 12B). This suggests that no significant displacement has accumulated on the 1st-phase faults during this stage.

Following a quiescent period of approximately 120 million years, 2nd-phase faults initiated (Fig. 12C and D). Maximum displacement (t_{max2}) between h30 and h45 suggests that faults were probably nucleated in this interval. Once initiated, they formed a relief at the free surface and triggered growth deposition of the 2nd syn-kinematic package. The correlation between the domain B and the 2nd syn-kinematic package is consistent with the displacement variation through syn-kinematic strata (Figs. 8 and 11). Domain B extends slightly below the 2nd syn-kinematic package suggesting that the throw gradient is also partly controlled by up-dip fault growth (Fig. 8). A higher gradient generally occurs within the syn-kinematic section and a distinct gradient increase is often observable at the upper most section (Fig. 9).

As the 2nd-phase faults kept up with the free surface during the 2nd syn-kinematic deposition, they also grew down-dip in order to maintain a proportional displacement accumulation (Fig. 12C and D). This process is predominantly restricted to the domain C and probably controlled the low throw gradients of the domain. The average gradient of 0.12 in this interval (Fig. 10) correlates to the tip gradients measured on the outcrop exposures (Wilkins and Gross, 2002).

Two end-member scenarios could be proposed for the down-dip growth of the 2nd-phase faults from t_{max2}: (i) The first model suggests a proportional growth (or radial growth) with gradual increase of fault length as throw accumulates (Fig. 12C). This model is based on the well-documented linear relationship between the fault dimensions and the displacement (Walsh and Watterson, 1988; Cowie and Scholz, 1992; Dawers et al., 1993; Schlische et al., 1996; Kim and Sanderson, 2005). (ii) The second model relies on the rapid establishment of the fault length, probably in the form of multiple vertical segments. Then, the displacement accumulates without a major change in the fault dimensions (Fig. 12D) (Walsh et al., 2002; Meyer et al., 2002; Morley, 2002).

While the 2nd-phase faults nucleated and grew during the 2nd-phase of extension, 1st-phase faults (i.e., the pre-existing zone of weaknesses) remained relatively inactive (Fig. 12C and D). Although there are variations among the structures, reactivation offsets of the 1st-phase faults are generally minor and less than the offsets accrued by the 2nd-phase faults. The lack of pervasive reactivation is well imaged by the presence of the displacement minimum (t_{min}) generally between h60 and h70 interval (Fig. 8). A slightly different throw distribution is observable on the north-dipping fault of the Vidalia structure where the t_{min} is almost eliminated due to significant displacement accumulation (Fig. 8B). This distribution illustrates a case of hard-linked connection between 1st- and 2nd-phase faults (Fig. 8B).

8.3. What controls the deformation style?

Fig. 7 depicts the first-order mechanical anisotropy of the sedimentary column with three mechanical stratigraphic units

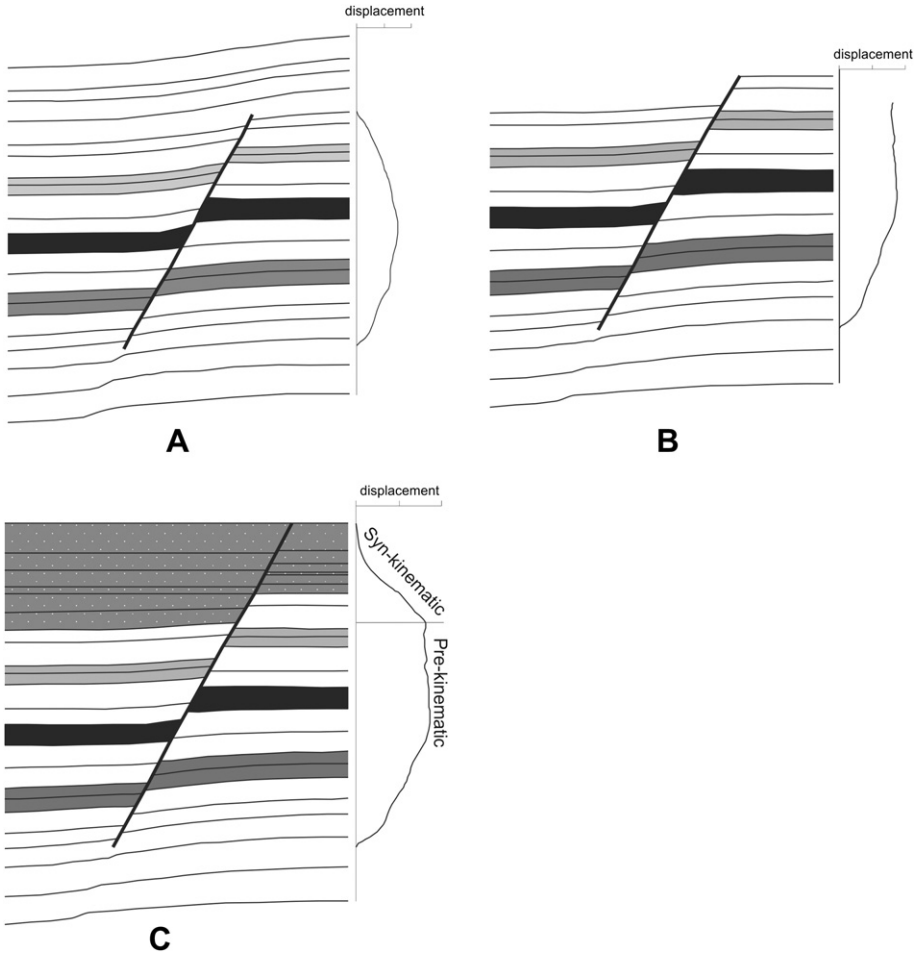

Fig. 11. Idealized displacement profile of a single fault surface: (A) a blind fault; (B) a fault with upper tip reaching to the free surface; and (C) (B) with syn-kinematic stratigraphic expansion.

(MU), the competent MU-1 and MU-3 separated by the incompetent MU-2. This mechanical layering is one of the key controls over the presented structural style and evolution of the hourglass structures (Fig. 12).

Prior to the 2nd-phase of extension, the upper tips of the 1st-phase faults probably remained below the KV marker within the incompetent MU-2 (Figs. 2 and 13). Incompetent rocks (e.g., shale) can accommodate more pre-failure strain than the competent rocks (e.g., sandstone or limestone) before the localization of deformation into a discrete slip plane (Donath, 1970; Ferrill and Morris, 2008). As a result, faults initially localize in competent layers (Schöpher et al., 2006) and incompetent layers with sufficient thickness can retard fault propagation or act as a mechanical barrier to fault growth (e.g., Ferrill et al., 2007; Ferrill and Morris, 2008; Morris et al., 2009). With the onset of the 2nd-phase of extension, the 1st-phase faults were possibly reactivated but up-dip propagation to the younger section were largely inhibited due to the ductile capacity of the MU-2, especially the KV-TE2 interval that completely buries the 1st-phase faults (Fig. 13).

While the 1st-phase faults were contained below a mechanical barrier formed by MU-2, the 2nd-phase faults were likely to nucleate and grow in the limestone dominated, competent MU-1 (Fig. 13). After the nucleation, the 2nd-phase fault grew down to the vicinity of horizontal barrier (i.e., MU-2) that also retarded the linkage of the 1st- and 2nd-phase fault systems. Thus, the upper section of the incompetent MU-2 remained as the displacement minimum and the main interval preventing the hard linkage of the two systems especially for the Laminaria and Corallina structures (Fig. 8A and C). Hard linkage and elimination of distinct throw minimum (t_{min}) in the Vidalia structure can be attributed to thinner claystone interval (between KV–KC) which may form less effective horizontal barrier at this structure (Figs. 8B and 13). The hard linkage may also be favored by almost parallel alignment of the 1st- and 2nd-phase fault systems (Fig. 6) which led to better kinematic coupling in the Vidalia structure.

Another potential control on the poor linkage of the 1st- and 2nd-phase fault systems relates to the evolution of tensional stress field in the region. The elastic flexure of the Australian plate when subducting under the Banda Arc is commonly considered as the cause of the 2nd-phase of extension (O'Brien et al., 1999; Londono and Lorenzo, 2004; Langhi et al., 2011) (Fig. 14). Langhi et al. (2011) modeled that the elastic flexure introduces localized extensional strain within the MU-1 that is probably controlled by the minor reactivation of the faults in MU-3 (Fig. 14). This suggests that the location, orientation and geometry of the 1st-phase faults controlled the localization of 2nd-phase strain in MU-1 and the grabens preferentially nucleated above the main horst blocks. The flexural extension is likely to form more 2nd-phase strain in the shallow section that gradually decreases downwards as portrayed by the distribution of Maximum Coulomb Shear Stress (MCSS; Jaeger and Cook, 1979) in Fig. 14C. This stress distribution also controls the detached nucleation and growth of the 2nd-phase faults from the 1st-phase faults and the linkage mechanism in-between.

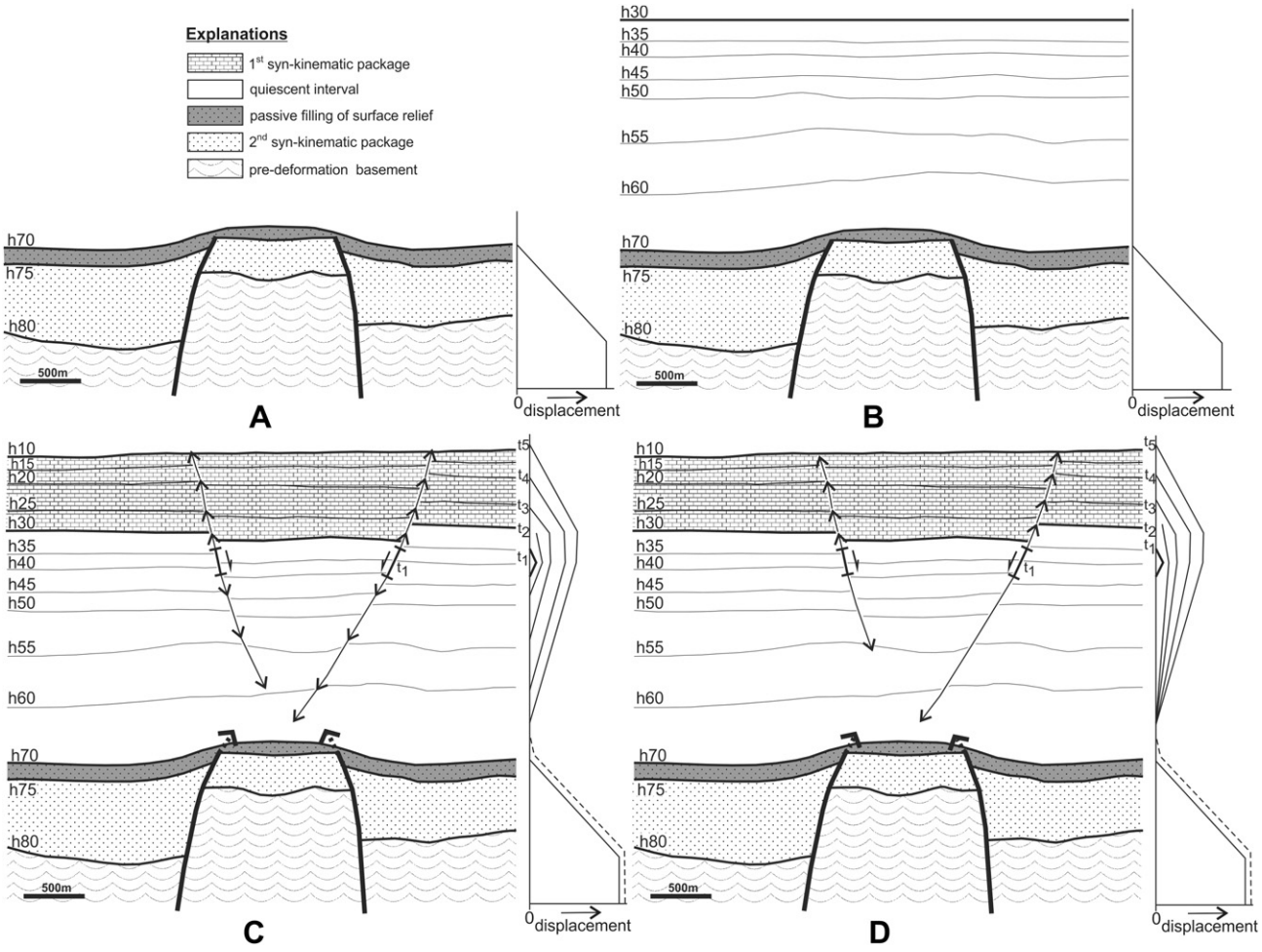

Fig. 12. Schematic model showing the evolution stages of the hourglass structures and displacement accumulated at each stage. (A) 1st-phase faulting with syn-kinematic package and throw domain A; (B) Quiescent period of approximately 120 My without fault activity and displacement accumulation; and (C) 2nd-phase faulting with syn-kinematic section and evolution of throw domains B and C. Model is based on the gradual down-dip fault growth; and (D) Same as C but with rapid down-dip fault growth. t_1–t_5 represents throw accumulation through time. Dashed line in throw profiles depicts minor reactivation of 1st-phase fault during the 2nd-phase of extension.

8.4. Hourglasses: time transgressive composite structures

Distinct deformation phases and their influence on the deposition are the main control over the systematic variation of displacement on the hourglass structures in the study area. Domains of positive displacement gradients (i.e., domains A and B in Fig. 8) are predominantly caused by the periods of syn-kinematic stratigraphic expansion. The negative gradient domain (i.e., Domain C in Fig. 8) is controlled by vertical detachment of the two systems due to combined effects of flexural extension and horizontal mechanical barrier to fault propagation. Therefore, the along-dip variations of the displacement and the location of displacement minimum are not directly related to the potential intersection zone of the oppositely dipping faults (Fig. 8C). This observation differs from some presented examples of the intersecting conjugate normal faults (e.g., Watterson et al., 1998).

In Fig. 15A, antithetic pairs F_1–F_1' and F_2–F_2' are independent conjugate fault systems formed by two separate phases of extension that are ~120 My apart. Although the location of the graben was probably controlled by the location of the underlying horst block, a caution is needed before integrating the two systems into a single crossing conjugate framework in the study area which may exist in other parts of the Timor Sea (e.g., Nicol et al., 1995). Note that synthetic pairs of F_1–F_2 and F_1'–F_2' cannot be considered as the same faults, because they have different ages, locally deviating strike orientations and different displacement characters due to independent displacement accumulations (Fig. 12). There are cases that the hard linkage is established between the synthetic faults of two systems as in the case of north-dipping fault of the Vidalia structure (Fig. 8B). The resulting fault is a time transgressive, composite structure with a displacement distribution reflecting the composite character of the fault plane. A model-based interpretation could propose that the south-dipping fault is offset by the north-dipping fault in the Vidalia structure (Fig. 8B) as suggested by the crossing conjugate fault models (Ferrill et al., 2000, 2009). But note that there is no continuum of displacement between the proposed offset segments of the south-dipping fault (Fig. 8B) as should be expected if this was once a continuous fault plane. Furthermore, north-dipping fault does not carry enough displacement near the h60 horizon which may correlate to the inferred offset of the south-dipping fault.

Another interpretation ambiguity might be to infer a hard linkage between the synthetic pairs of 1st- and 2nd-phase faults between h60 and h70 in the Corallina structure (Fig. 8A) and to interpret the throw minimum (t_{min}) as resulting from the low-angle connection between the two fault systems. However, the trends of throw gradient extend above and below h60–h70 interval where fault interpretations show no dip variations. In

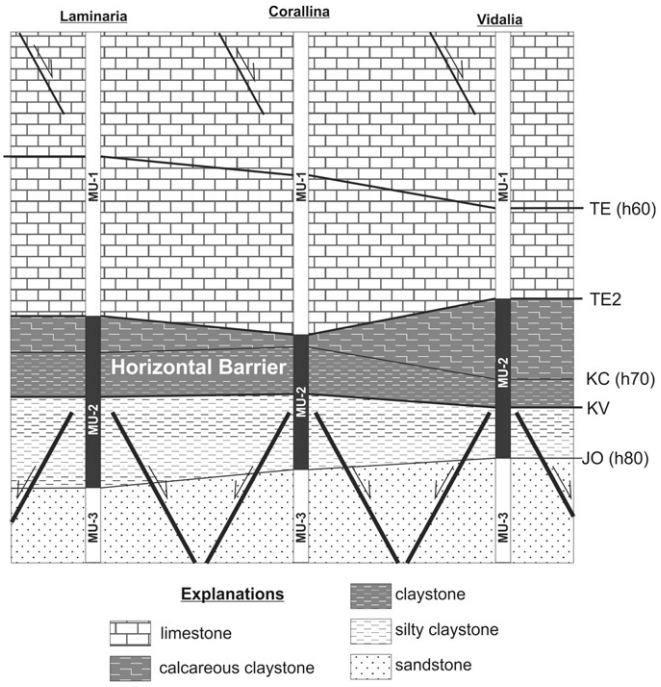

Fig. 13. Schematic diagram showing mechanical stratigraphic units and location of horizontal barrier (gray shaded area) detaching the 1st- and 2nd-phase fault systems. See Fig. 7 for the discrimination of mechanical units (MU).

Laminaria structure, some fault intersection zones correlate with displacement maximum (t_{max2}; Fig. 8C) and the displacement minimum still occurs in the h60–h70 interval where there is no fault intersection.

These observations suggest that the crossing conjugate fault models are not applicable to the investigated hourglass structures in the Laminaria High area and the observed systematic variation of displacement is not controlled by the crossing conjugate geometry.

8.5. Implications of the presented hourglass model on trap integrity

Hydrocarbon leakage in the Laminaria High area is generally attributed to reactivation of the 1st-phase faults and upward remigration relating to a fault seal problem (Lisk et al., 1998; O'Brien et al., 1999; De Ruig et al., 2000; Gartrell et al., 2005, 2006; Langhi et al., 2010). The predicted membrane seal quality of the top seal is high (De Ruig et al., 2000 and references therein) and the absence of aquifer overpressures support low top-seal failure risk. In the presented model with two detached fault systems, the fault tips concentrate to the interval of throw minimum which corresponds to the regional top seal. These tips are Mode II fault tips with tip lines oriented orthogonal to the sense of slip. A variety of tip damage zones is defined for Mode II tips; these being wing cracks, horsetail fractures, synthetic branch faults and antithetic branch faults (Atkinson, 1987; Kim et al., 2004). They are widely variable in terms of scale from millimeters to hundreds of kilometers and usually extend well beyond the actual tip of the fault zone. Therefore, even though the top seal is an interval with high ductile capacity, subseismic scale, distributed tip front deformation zone can develop across the interval and form subseismic fracture systems impacting on the flow behavior of the top seal.

Fig. 14B shows a forward deformation model that captures the scale, detached fault style, and mechanical stratigraphy of the hourglass structures in the study area. The slip on the 2nd-phase faults with inactive horst blocks concentrates the high values of the maximum Coulomb shear stress (Jaeger and Cook, 1979) into the tip zone of the 2nd-phase faults. If we consider the maximum Coulomb

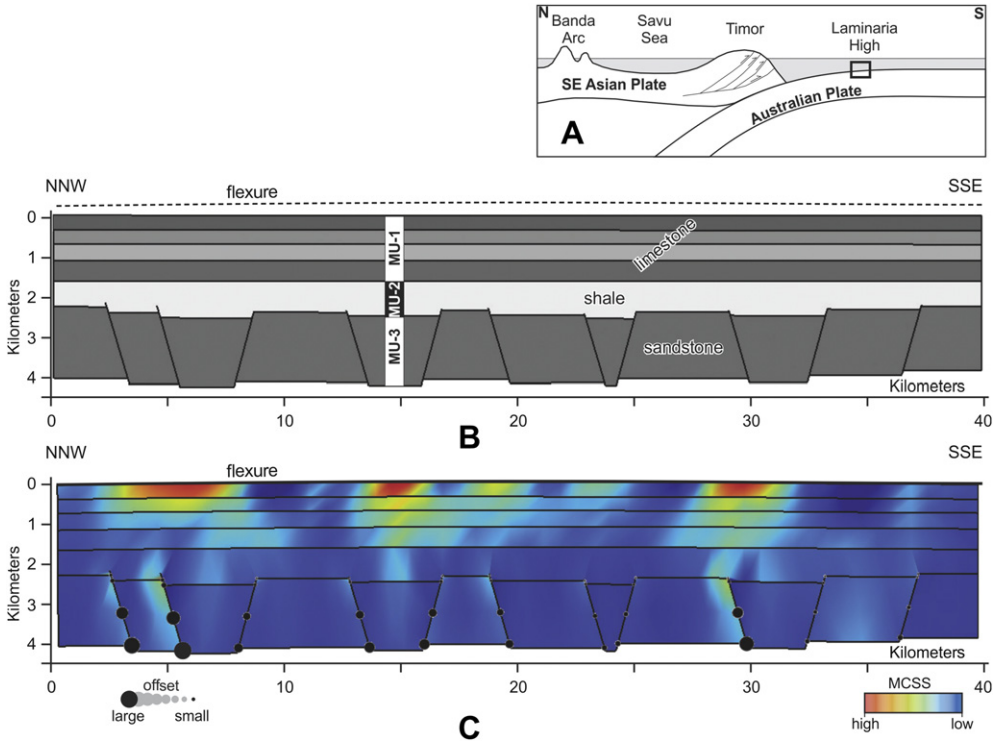

Fig. 14. Forward deformation model with mechanically anisotropic sedimentary column and buried horst-graben blocks. From Langhi et al. (2011) (A) Schematic diagram showing lithospheric flexure of the Australian Plate due to trust loading at Timor (Fig. 4). (B) Six-layer model with mechanical stratigraphic units MU-1–MU-3 as in Fig. 7. The model is deformed by folding it to fit the theoretical flexure of the Timor Sea foreland (dashed line). (B) Distribution of Maximum Coulomb Shear Stress (MCSS; Jaeger and Cook, 1979) on the deformed model as a proxy for 2nd-phase fault location and density.

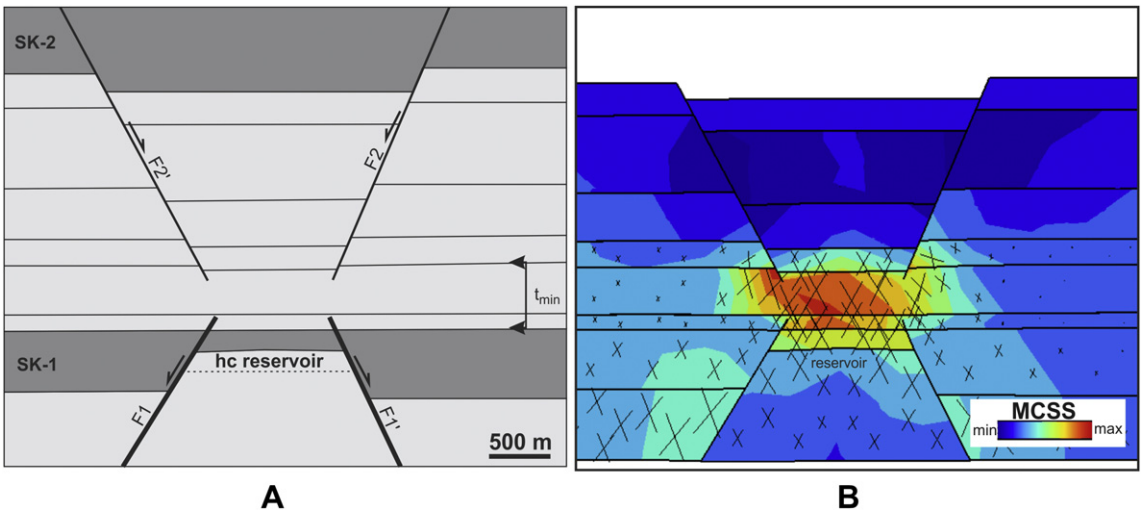

Fig. 15. (A) A schematic diagram of the 1st-phase (F_1 and F_1') and 2nd-phase (F_2 and F_2') faults in the study area. (B) Forward deformation model of the schematic configuration in (A) capturing the deformation and scale of hourglass structures in the study area. Color illustrates the distribution of Maximum Coulomb Shear Stress (MCSS; Jaeger and Cook, 1979). X shows the orientation of optimum conjugate failure planes with size scaled to MCSS. The model was computed using Dynel 2D (Maerten and Maerten, 2006).

shear stress as a proxy to location and density of subseismic scale fracturing (e.g., Maerten and Maerten, 2006; Crider and Pollard, 1998), the most intense tip deformation is likely to take place immediately above the reservoir bearing horst block, mostly within the top-seal section (Fig. 15B). Stress perturbation near fault tips is known to enhance fracture permeability by opening and shearing and therefore could risk the top-seal integrity (e.g., Tamagawa and Pollard, 2008; Langhi et al., 2010). Leakage through top seal could also explain the oil–water contact in the Corallina structure that is locally above the fault – top reservoir intersection by 20–30 m (Gartrell et al., 2006).

9. Conclusions

Analysis of along-dip displacement distribution can be effectively used to reconstruct the slip and growth history of faults and is particularly useful for composite structures which span through multiple deformation phases. Knowledge of syn-kinematic sections and mechanical stratigraphic units are the other preliminary inputs to these analyses as they have an impact on displacement gradients.

The investigated hourglass structures in the Laminaria High area are composite structures with bounding faults evolving across 1st- and 2nd-phases of extension (Fig. 2). Fault offset varies systematically and a displacement minimum commonly occurs within an incompetent unit that detaches the 1st-phase horst-bounding and 2nd-phase graben-bounding structures. Displacement variation and style of deformation are in agreement with the complex evolution history of the structures and the applicability of crossing conjugate fault models (Ferrill et al., 2000, 2009) to the hourglass structures is limited in the study area. The proposed evolution model concentrates fault tips and related stress perturbations into the minimum displacement zone which partly correlates to the regional top seal. Soft interactions among fault tips and the interference of stress perturbations may create complex ductile (at the seismic scale) deformation zone and increase vertical permeability through this interval risking the top-seal integrity.

Acknowledgments

We thank David A. Ferrill, Conrad Childs and Tom Blenkinsop for helpful reviews that greatly improved the original manuscript. Julian Strand is thanked for fruitful discussions; Roxar (RMS), Badley Geoscience (Trap Tester) and Igeoss (Dynel 2D) are thanked for providing software licenses and support.

References

AGSO, 1994. Deep reflections on the north west shelf: changing perceptions of basin formation. In: Purcell, P.G., Purcell, R.R. (Eds.), The Sedimentary Basins of Western Australia. The Sedimentary Basins of Western Australia 1, Proceedings of the Petroleum Exploration Society of Australia Symposium, Perth, pp. 63–76.
Anderson, E.M., 1951. The Dynamics of Faulting and Dyke Formation with Applications to Britain. Oliver & Boyd, Edinburgh.
Atkinson, B.K., 1987. Introduction to fracture mechanics and its geophysical applications. In: Atkinson, B.K. (Ed.), Fracture Mechanics of Rock. Academic Press, London, pp. 1–26.
Baillie, P.W., Powell, C.M., Li, Z.X., Ryall, A.M., 1994. The tectonic framework of Western Australia's neoproterozoic to recent sedimentary basins. In: Purcell, P.G., Purcell, R.R. (Eds.), The Sedimentary Basins of Western Australia 1, Proceedings of the Petroleum Exploration Society of Australia Symposium, Perth, pp. 45–62.
Barnett, J.A.M., Mortimer, J., Rippon, J.H., Walsh, J.J., Watterson, J., 1987. Displacement geometry in the volume containing a single normal fault. American Association of Petroleum Geologists Bulletin 71, 925–937.
Baudon, C., Cartwright, J., 2008a. Early stage evolution of growth faults: 3D seismic insight from the Levant Basin, Eastern Mediterranean. Journal of Structural Geology 30, 888–898.
Baudon, C., Cartwright, J., 2008b. The kinematics of reactivation of normal faults using high resolution throw mapping. Journal of Structural Geology 30, 1072–1084.
Borel, G.D., Stampfli, G.M., 2002. Geohistory of the NW Shelf: a tool to assess the Phanerozoic motion of the Australian Plate. In: Keep, M., Moss, S.J. (Eds.), The Sedimentary Basins of Western Australia 3. Proceedings of the Petroleum Exploration Society of Australia Symposium, Perth, pp. 119–128.
Bradley, D.C., Kidd, W.S.F., 1991. Flexural extension of the upper continental crust in collisional foredeeps. Geological Society of America Bulletin 103, 1416–1438.
Bretan, P.G., Nicol, A., Walsh, J.J., Watterson, J., July 1996. Origin of some conjugate or "X" fault structures. The Leading Edge, 812–816.
Cartwright, J.A., Mansfeld, C.M., 1998. Lateral displacement variations and lateral tip geometry of normal faults in the Canyonlands National Park, Utah. Journal of Structural Geology 20, 3–19.
Charlton, T.R., Barber, A.J., Barkham, S.T., 1991. The structural evolution of the Timor collision complex, eastern Indonesia. Journal of Structural Geology 13, 489–500.
Charlton, T.R., 2000. Tertiary evolution of the eastern Indonesia collision complex. Journal of Asian Earth Sciences 18, 603–631.
Childs, C., Easton, S.J., Vendeville, B.C., Jackson, M.P.A., Lin, S.T., Walsh, J.J., Watterson, J., 1993. Kinematic analysis of faults in a physical model of growth faulting above a viscous salt analogue. Tectonophysics 228, 313–329.
Childs, C., Nicol, A., Walsh, J.J., Watterson, J., 1996. Growth of vertically segmented normal faults. Journal of Structural Geology 18, 1389–1397.
Childs, C., Watterson, J., Walsh, J.J., 1995. Fault overlap zones within developing normal fault systems. Journal of Geological Society (London) 152, 535–549.

Çiftçi, N.B., Bozkurt, E., 2009. Pattern of normal faulting in the Gediz Graben. Tectonophysics 473, 234–260.
Cowie, P.A., Scholz, C.H., 1992. Displacement–length scaling relationship for faults: data synthesis and discussion. Journal of Structural Geology 14, 1149–1156.
Crider, J.G., Pollard, D.D., 1998. Fault linkage: three-dimensional mechanical interaction between echelon normal faults. Journal of Geophysical Research 103, 24373–24391.
Dawers, N.H., Anders, M.H., Scholz, C.H., 1993. Growth of normal faults: displacement–length scaling. Geology 21, 1107–1110.
De Ruig, M.J., Trupp, M., Bishop, D.J., Kuek, D., Castillo, D.A., 2000. Fault architecture and the mechanics of fault reactivation in the Nancar Trough/Laminaria area of the Timor Sea, northern Australia. Australian Petroleum Production and Exploration Association Journal 40, 174–193.
Donath, F.A., 1970. Some information squeezed out of rock. American Scientist 58, 54–72.
Edwards, H., Crosby, J., David, N., Loader, C., Westlake, S., 2005. Australian Megasurveys – the key to new discoveries in maturing areas? Australian Petroleum Production and Exploration Association Journal 45, 407–420.
Ferrill, D.A., Morris, A.P., 2008. Fault zone deformation controlled by carbonate mechanical stratigraphy, Balcones fault system, Texas. American Association of Petroleum Geologists Bulletin 92, 359–380.
Ferrill, D.A., Morris, A.P., McGinnis, R.N., 2009. Crossing conjugate normal faults in field exposures and seismic data. American Association of Petroleum Geologists Bulletin 93, 1471–1488.
Ferrill, D.A., Morris, A.P., Smart, K.J., 2007. Stratigraphic control on extensional fault propagation folding: Big Brushy Canyon monocline, Sierra Del Carmen, Texas. In: Jolley, S.J., Wals, J.J., Knipe, R.J. (Eds.), Structurally Complex Reservoirs. Geological Society (London) Special Publication 292, pp. 203–217.
Ferrill, D.A., Morris, A.P., Stamatakos, J.A., Sims, D., 2000. Crossing conjugate normal faults. American Association of Petroleum Geologists Bulletin 84, 1543–1559.
Gartrell, A., Bailey, W.R., Brincat, M., 2005. Strain localisation and trap geometry as key controls on hydrocarbon preservation in the Laminaria High area. Australian Petroleum Production and Exploration Association Journal 45, 477–492.
Gartrell, A., Bailey, W.R., Brincat, M., 2006. A new model for assessing trap integrity and oil preservation risks associated with postrift fault reactivation in the Timor Sea. American Association of Petroleum Geologists Bulletin 90, 1921–1944.
George, S.C., Ruble, T.E., Volk, H., Lisk, M., Brincat, M.P., Dutkiewicz, A., Ahmed, M., 2004. Comparing the geochemical composition of fluid inclusion and crude oils from wells on the Laminaria High, Timor Sea. In: Ellis, G.K., Baillie, P.W., Munson, T.J. (Eds.), Timor Sea Petroleum Geoscience. Proceedings of the Timor Sea Symposium, pp. 203–230.
Horsrud, P., 2001. Estimating mechanical properties of shale from empirical correlations. SPE Drilling and Completion 16, 68–73.
Jaeger, J.C., Cook, N.G.W., 1979. Fundamentals of Rock Mechanics. Chapman and Hall, New York.
Keep, M., Clough, M., Langhi, L., 2002. Neogene tectonic and structural evolution of the Timor Sea region, NW Australia. In: Keep, M., Moss, S.J. (Eds.), The Sedimentary Basins of Western Australia 3. Proceedings of the Petroleum Exploration Society of Australia Symposium, Perth, pp. 341–353.
Kennard, J.M., Deighton, I., Edward, D.S., Colwell, J.B., O'Brien, G., Boreham, C.J., 1999. Thermal history modelling and transient heat pulses: new insights into hydrocarbon expulsion and "hot flushes" in the Vulcan subbasin, Timor Sea. Australian Petroleum Production and Exploration Association Journal 39, 177–207.
Kim, Y.S., Sanderson, D.J., 2005. The relationship between displacement and length of faults: a review. Earth Science Reviews 68, 317–334.
Kim, Y.S., Peacock, D.C.P., Sanderson, D.J., 2004. Fault damage zones. Journal of Structural Geology 26, 503–517.
Labutis, V.R., Ruddock, A.D., Calcraft, A.P., 1998. Stratigraphy of the Sahul platform. Australian Petroleum Production and Exploration Association Journal 38, 115–136.
Langhi, L., Ciftci, N.B., Borel, G.D., 2011. Impact of lithospheric flexure on the evolution of shallow faults in the Timor foreland system. Marine Geology 284, 40–54.
Langhi, L., Zhang, Y., Gartrell, A., Underschultz, J.R., Dewhurst, D.N., 2010. Evaluating hydrocarbon trap integrity during fault reactivation using geomechanical 3D modelling: an example from the Timor Sea, Australia. American Association of Petroleum Geologists Bulletin 94, 567–591.
Lisk, M., Brincat, M.P., Eadington, P.J., O'Brien, G.W., 1998. Hydrocarbon charge in the Vulcan subbasin. In: Purcell, P.G., Purcell, R.R. (Eds.), The Sedimentary Basins of Western Australia. Proceedings of Petroleum Exploration Society of Australia Symposium 2, pp. 287–303.
Londono, J., Lorenzo, J.M., 2004. Geodynamics of continental plate collision during late tertiary foreland basin evolution in the Timor Sea: constraints from foreland sequences, elastic flexure and normal faulting. Tectonophysics 392, 37–54.
Longley, I.M., Buessenschuett, C., Clydsdale, L., Cubitt, C.J., Davis, R.C., Johnson, M.K., Marshall, N.M., Murray, A.P., Somerville, R., Spry, T.B., Thompson, N.B., 2002. The North West Shelf of Australia: a woodside perspective. In: Keep,, M., Moss,, S. (Eds.), The Sedimentary Basins of Western Australia. Proceedings of Petroleum Exploration Society of Australia Symposium 3, pp. 27–88.
Maerten, L., Maerten, F., 2006. Chronological modelling of faulted and fractured reservoirs using geomechanically based restoration: technique and industry applications. American Association of Petroleum Geologists Bulletin 90, 1201–1226.
Meyer, V., Nicol, A., Childs, C., Walsh, J.J., Watterson, J., 2002. Progressive localisation of strain during the evolution of a normal fault population. Journal of Structural Geology 24, 1215–1231.
Morley, C.K., 1999. Patterns of displacement along large normal faults: implications for basin evolution and fault propagation, based on examples from East Africa. American Association of Petroleum Geologists Bulletin 83, 613–634.
Morley, C.K., 2002. Evolution of large normal faults: evidence from seismic reflection data. American Association of Petroleum Geologists Bulletin 86, 961–978.
Morris, A.P., Ferrill, D.A., McGinnis, R.N., 2009. Mechanical stratigraphy and faulting in Cretaceous carbonates. American Association of Petroleum Geologists Bulletin 93, 1459–1470.
Nicol, A., Walsh, J.J., Watterson, J., Bretan, P.G., 1995. Three-dimensional geometry and growth of conjugate normal faults. Journal of Structural Geology 17, 847–862.
O'Brien, G.W., Etheridge, M.A., Willcox, J.B., Morse, M., Symonds, P., Norman, C., Needham, D.J., 1993. The structural architecture of the Timor Sea, northwestern Australia; implications for basin development and hydrocarbon exploration. Australian Petroleum Production and Exploration Association Journal 33, 258–278.
O'Brien, G.W., Lisk, M., Duddy, I.R., Hamilton, J., Woods, P., Cowley, R., 1999. Plate convergence, foreland development and fault reactivation; primary controls on brine migration, thermal histories and trap breach in the Timor Sea, Australia. Marine and Petroleum Geology 16, 533–560.
Patillo, J., Nicholls, P.J., 1990. A tectonostratigraphic framework for the Vulcan Graben, Timor Sea region. Australian Petroleum Production and Exploration Association Journal 30, 27–51.
Preston, J.C., Edwards, D.S., 2000. The petroleum geochemistry of oils and source rocks from the northern Bonaparte Basin, offshore northern Australia. Australian Petroleum Production and Exploration Association Journal 40, 257–281.
Purcell, P.G., Purcell, R.R., 1988. The North West Shelf, Australia – an introduction. In: Purcell, P.G., Purcell, R.R. (Eds.), The North West Shelf, Australia. Proceedings of the Petroleum Exploration Society of Australia, pp. 2–15.
Ramsey, J.G., Huber, M.I., 1987. The Techniques of Modern Structural Geology. In: Folds and Fractures, vol. 2. Academic Press Inc., London.
Schlische, R.W., Young, S.S., Ackermann, R.V., Gupta, A., 1996. Geometry and scaling relations of a population of very small rift-related normal faults. Geology 24, 683–686.
Schöpher, M.P.J., Childs, C., Walsh, J.J., 2006. Localisation of normal faults in multilayer sequences. Journal of Structural Geology 28, 816–833.
Shuster, M.W., Eaton, S., Wakefield, L.L., Kloosterman, H.J., 1998. Neogene tectonics, Greater Timor Sea, offshore Australia: implications for trap risk. Australian Petroleum Production and Exploration Association Journal 38, 351–379.
Smith, G.C., Tilbury, L.A., Chatfield, A., Senycia, P., Thompson, N., 1996. Laminaria – a new Timor Sea discovery. Australian Petroleum Production and Exploration Association Journal 36, 12–28.
Tamagawa, T., Pollard, D.D., 2008. Fracture permeability created by perturbed stress fields around active faults in a fractured basement reservoir. American Association of Petroleum Geologists Bulletin 92, 743–764.
Taylor, S.K., Nicol, A., Walsh, J.J., 2008. Displacement loss on growth faults due to sediment compaction. Journal of Structural Geology 30, 394–405.
Walsh, J.J., Watterson, J., 1987. Distributions of cumulative displacement and seismic slip on a single normal fault surface. Journal of Structural Geology 9, 1039–1046.
Walsh, J.J., Watterson, J., 1988. Analysis of the relationship between the displacements and dimensions of faults. Journal of Structural Geology 10, 239–247.
Walsh, J.J., Nicol, A., Childs, C., 2002. An alternative model for the growth of faults. Journal of Structural Geology 24, 1669–1675.
Watterson, J., Nicol, A., Walsh, J.J., 1998. Strains at the intersections of synchronous conjugate normal faults. Journal of Structural Geology 20, 363–370.
Whittam, D.B., Norvick, M.S., McIntyre, C.L., 1996. Mesozoic and Cainozoic tectonostratigraphy of western ZOCA and adjacent areas. Australian Petroleum Production and Exploration Association Journal 36, 209–232.
Wilkins, S.J., Gross, M.R., 2002. Normal fault growth in layered rocks at Split Mountain, Utah: influence of mechanical stratigraphy on dip linkage, fault restriction and fault scaling. Journal of Structural Geology 24, 1413–1429.
Woods, E.P., 1988. Extensional structures of the Jabiru Terrace, Vulcan Sub-basin. In: Purcell, P.G., Purcell, R.R. (Eds.), The Northwest Shelf Australia. Proceedings of the Petroleum Exploration Society of Australia, pp. 311–330.
Woods, E.P., 1992. Vulcan sub-basin fault styles – implications for hydrocarbon migration and entrapment. Australian Petroleum Production and Exploration Association Journal 32, 138–158.
Yeates, A.N., Bradshaw, M.T., Dickins, J.M., Brakel, A.T., Exon, N.F., Langford, R.P., Mulholland, S.M., Totterdell, J.M., Yeung, M., 1987. The Westralian Superbasin: an Australian link with Tethys. In: McKenzie,, K.G. (Ed.), Shallow Tethys 2, pp. 199–213.